Aqueous electrocatalytic N_2 reduction under ambient conditions

Na Cao and Gengfeng Zheng (✉)

Laboratory of Advanced Materials, Department of Chemistry and Shanghai Key Laboratory of Molecular Catalysis and Innovative Materials, Collaborative Innovation Center of Chemistry for Energy Materials, Fudan University, Shanghai 200438, China

ABSTRACT

Recently, the electrochemical N_2 reduction reaction (NRR) in aqueous electrolytes at ambient temperature and pressure has demonstrated its unique advantages and potentials. The reactants are directly derived from gaseous N_2 and water, which are naturally abundant, and NH_3 production is important for fertilizers and other industrial applications. To improve the conversion yield and selectivity (mainly competing with water reduction), electrocatalysts must be rationally designed to optimize the mass transport, chemisorption, and transduction pathways of protons and electrons. In this review, we summarize recent progress in the electrochemical NRR. Studies of electrocatalyst designs are summarized for different categories, including metal-based catalysts, metal oxide-derived catalysts, and hybrid catalysts. Strategies for enhancing the NRR performance based on the facet orientation, metal oxide interface, crystallinity, and nitrogen vacancies are presented. Additional system designs, such as lithium-nitrogen batteries, and the solvent effect are introduced. Finally, existing challenges and prospects are discussed.

1 Introduction

N_2 is the most abundant molecule in the atmosphere. It is one of the most inert chemical species because of the high bond energy of the N≡N triple bond (941 kJ·mol⁻¹), its lack of a dipole moment, and its low polarizability [1]. Industrial-scale reduction of N_2 to NH_3 is predominantly carried out via the Haber-Bosch process, developed by Fritz Haber and Carl Bosch over a century ago, using Fe-based catalysts at both high temperature (350–550 ℃) and high pressure (150–300 atm) [2]. Today, about 80% of NH_3 produced from this reaction is converted

to fertilizers, which have contributed to human population growth on Earth [3]. In addition to agriculture, NH_3 is substantially used in the plastic and textile industries, and as a stable hydrogen carrier [4–9]. Three typical pathways for nitrogen fixation exist: azotobacter nitrogen fixation (a natural biological process), the Haber-Bosch process (the first anthropogenic pathway), and electrocatalysis (Fig. 1(a)).

Green biological nitrogen fixation could scarcely meet the current tremendous needs of the fertilizer industry. The Haber-Bosch process consumes a high amount of energy to produce NH_3 and provides a relatively low equilibrium conversion yield of ~ 15%

[3]. At present, over 1% of the total global fossil energy is used for NH_3 formation. In addition, the H_2 molecules used in the reactions are mainly obtained from dissociating natural gas or other fossil fuels, causing significant CO_2 emissions into the atmosphere [10]. Furthermore, either the Haber-Bosch process or the newer Kellogg advanced NH_3 process [11] requires substantially centralized infrastructures, which are largely deficient in many less-developed areas of the world [12]. Thus, substantial research efforts have been dedicated to pursuing N_2 fixation under milder conditions, such as mimicking biological nitrogenase [13, 14], or using photochemical and electrochemical systems [15–19]. For instance, molybdenum-based transition metal complexes can reduce N_2 to NH_3 at ambient pressure and temperature [20]. Alternatively, steam electrolysis has been reported to synthesize NH_3 from N_2 in a molten hydroxide suspension of nanosized Fe_2O_3 [8]. However, many drawbacks still exist for all the methods reported to date, including low yields and slow kinetics [21], expensive electrolytes [22], or harsh reaction conditions [23].

The heterogeneous electrocatalytic N_2 reduction reaction (NRR) to NH_3 in an aqueous electrolyte, ideally powered by clean/renewable energies (e.g., solar or wind), represents an attractive approach for N_2 fixation. N_2 molecules from air are directly used as the nitrogen source, and the protons are provided by electrical water splitting. Electrons are driven toward the electrocatalyst surface by an applied voltage. H_2O is selected to ubiquitously supply protons because of its lower energy demand than the traditional Haber-Bosch process using H_2 as a hydrogen source [24]. In addition, the essential proton transfer process can also be tuned using different aqueous electrolytes, which can improve the NRR selectivity [1]. This process may enable a more sustainable production of NH_3 for fertilizers and carbon-free energy carriers.

The aqueous NRR process is typically studied in a three-electrode system, where the major anodic reaction is the oxidation of water molecules, also known as the oxygen evolution reaction. On the cathode side, N_2 gas is supplied as a feed gas stream. The cathodic reaction depends on the type of aqueous electrolyte (acidic or alkaline) [25]. In an acidic aqueous electrolyte, the produced protons on the counter electrode are directly transported through a proton exchange membrane toward the cathode, where NH_3 molecules are formed. Thus, the two half reactions in an acidic solution are described as [10, 26]

Anodic (oxidation)

$$3H_2O \rightarrow 6H^+ + 1.5O_2 + 6e^- \qquad (1)$$

Cathodic (reduction)

$$6H^+ + N_2 + 6e^- \rightarrow 2NH_3 \qquad (2)$$
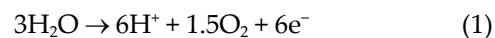
In an alkaline electrolyte, the cathodic half reaction follows another pathway, in which N_2 directly combines with water and electrons to form NH_3. The produced OH^- ions pass through an anion exchange membrane toward the cathode side to be oxidized to O_2, represented as follows [27]
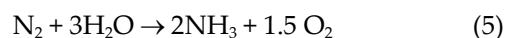
Anodic (oxidation)

$$6OH^- \rightarrow 1.5O_2 + 6e^- + 3H_2O \qquad (3)$$

Cathodic (reduction)

$$N_2 + 6H_2O + 6e^- \rightarrow 2NH_3 + 6OH^- \qquad (4)$$
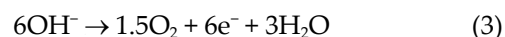
In either case, the overall reaction is shown as [28]

$$N_2 + 3H_2O \rightarrow 2NH_3 + 1.5\ O_2 \qquad (5)$$

The major side reaction of the NRR is the reduction of water, also known as the hydrogen evolution reaction (HER), in which water (H_2O, protons or hydroxide ion) gains electrons to be reduced to gaseous H_2 [29, 30]. As a result, the faradaic efficiency (FE) of the NRR is significantly suppressed—typically only a few percent or even below 1% [13]. There are two general strategies to improve the properties of the NRR. One is to enhance the specific NRR activity of the electrocatalysts, for example, by introducing active crystal planes [27], defects or vacancies, a specific porous structure [31], or a hybrid material interface [32]. With higher densities of exposed active sites, the chemisorption of N_2 molecules can be enhanced, thus enhancing the NRR activity. The other strategy is to inhibit the competitive HER, for example, by tuning the electrolyte [33], enhancing N_2 mass transfer, or reducing water transport [34].

The mechanism of the electrocatalytic reduction of N_2 is complicated and has not been completely elucidated;

it may depend on the catalytic surface and applied voltages [35, 36]. Generally, the NRR mechanism is considered via three pathways [35], namely, the associative alternating pathway, associative distal pathway, and dissociative pathway [10, 37]. The associative alternating pathway (Fig. 1(b), top) indicates that both the distal and proximal N atoms are protonated before N–N bond dissociation. In other words, the successive cleavage of the N–N bond and formation of a new N–H bond take place with consecutive addition of protons. Thus, the first NH_3 molecule is formed, and subsequently, another NH_3 can be obtained [38]. In contrast, for the associative distal pathway (Fig. 1(b), middle), the successive hydriding process occurs preferentially at the distal N atoms to form NH_3. This mechanism includes the following three steps [39]. First, the N_2 molecule is adsorbed on the surface, which serves as the active site and leads to cleavage of the first N–N bond of the stable N≡N triple bond. Second, two active protons in the electrolyte associate with the distal N atoms and two electrons to form the first NH_3 molecule. Third, consecutive addition of protons occurs at the proximal N atoms to form the other NH_3 molecule. Moreover, the dissociative pathway (Fig. 1(b), bottom) is also considered in the NRR mechanism, such as in the Haber-Bosch process. N≡N triple bond cleavage takes place before the hydriding process, leaving N adatoms solely on the catalyst surface. The N adatoms undergo consecutive hydrogenation, and are finally converted to NH_3.

In this review, we will summarize the recent progress in electrocatalytic N_2 reduction under ambient conditions.

Electrocatalysts are generally categorized into several groups, including metal-based, metal oxide [40], polymer, and hybrid catalysts [41]. Several strategies are discussed for promoting the catalyst activities and selectivities by introducing more exposed active sites [42], such as crystal planes [43], defects [44], and vacancies [45]. In addition, the effect of electrolytes on the NRR activity and selectivity, as well as Li-N_2 battery systems are also presented. Finally, existing challenges and future perspectives are discussed.

2 Metal-based catalysts

2.1 Theoretical calculations

Many metal-based catalysts, such as Fe, Mo, Ru, and Rh, have been investigated in pioneering theoretical and experimental studies [46, 47]. In 2012, Nørskov and coworkers carried out density functional theory (DFT) calculations of early transition metal surfaces to reveal the correlation between the adsorption of surface N species and the catalytic performance of NH_3 formation in an acidic electrolyte [35]. In the models, the activities of the stepped surface and close-packed surface of catalysts were also compared. The stepped surfaces of the metal catalysts were simulated using periodically repeating layer cells of a specific crystal plane, of which the top two layers were relaxed to create a strip island. For the close-packed metal surface, the specific crystal planes were simulated by fixing the top two layers. The chemisorption energies of N and H adatoms on the close-packed metal surface are
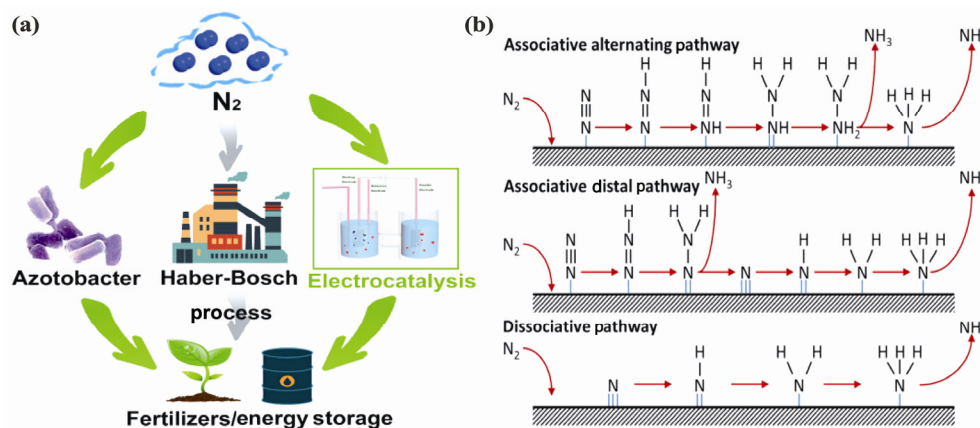
Figure 1 (a) Three typical pathways of nitrogen fixation and their applications. (b) Generic mechanisms for N_2 reduction to NH_3 on heterogeneous catalysts. Reproduced with permission from Ref. [10], © Elsevier B.V. 2017.
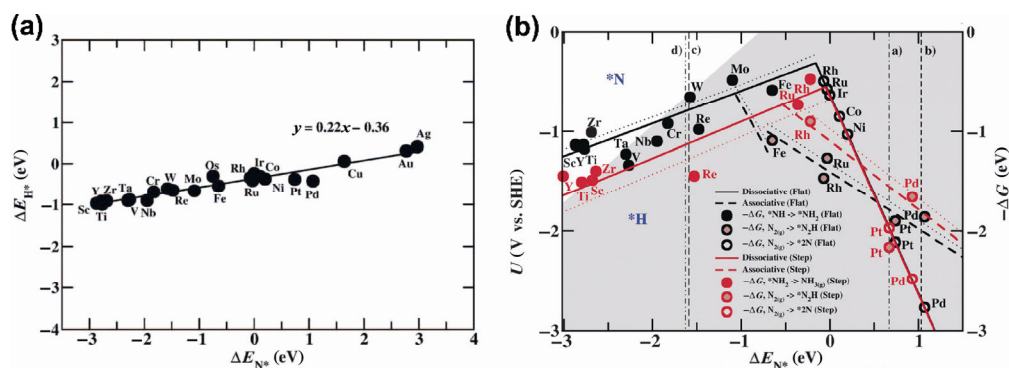
Figure 2 (a) Adsorption energy of H adatoms as a function of the chemisorption energy of N adatoms on selected, close-packed transition metal surfaces. (b) Combined volcano diagrams (lines) for the flat (black) and stepped (red) transition metal surfaces for reduction of N_2 using a Heyrovsky-type reaction, without (solid lines) and with (dotted lines) H-bonding effects. Reproduced with permission from Ref. [35], © The Royal Society of Chemistry 2012.

plotted and compared (Fig. 2(a)), which reveals a linear correlation of these adsorption energies. In addition, a volcano diagram is displayed, including dissociative (solid lines) and associative (dashed lines) mechanisms, both modelled on stepped (red lines) and flat (black lines) metal catalyst surfaces (Fig. 2(b)). The first proton transfer process (dashed lines) determines the NRR onset potentials, while the NRR activity depends on the N_2 splitting capability (solid lines) of the electrocatalysts.

This study further indicated that the HER is a main and critical side reaction for the NRR, whereas the selectivity of the catalyst is strongly affected by the attachment of the active centers (i.e., to N or H atoms). The authors suggest that the optimized NRR catalysts should have identical nitrogen binding energies for the intermediates that are close to the theoretical equilibrium potential. Based on their results, the authors concluded that Sc, Y, Ti, and Zr metal surfaces bind N adatoms more strongly than H adatoms, and can produce a significant NH_3 yield rather than competing H_2. Most recently, a DFT analysis of NH_3 synthesis using Ru, Os, and Rh catalysts was performed by Nakai et al. In this work, the Ru catalysts showed the best NH_3 generation properties. The authors ascribed the high activity to three key factors: The activation barrier (E_a), coverage of the surface vacancy sites, and number of step sites [48].

2.2 Molecular catalysts

For conventionally structured NRR catalysts, Pickett et al. studied electrosynthesis of NH_3 at room temperature by protolysis of cis-[W(N_2)$_2$(PMe$_2$Ph)$_4$] in 1985 [49].

The electrochemical N_2 conversion under ambient temperature and pressure involved a sequence of protonation and electronation processes.

One of the earliest studies of the NRR under ambient temperature and pressure was reported by Furuya et al. in 1989, in which iron phthalocyanine was used as the catalyst [50]. In this work, N atoms and protons were provided by N_2 and water, respectively. The authors further investigated a series of metal phthalocyanine catalysts, including Ti, Fe, Ni, Co, Pd, Pt, Cu, Zn, Al, Ga, In, Sn, and Pb, for N_2 electrochemical reduction under ambient pressure and temperature in 1 M KOH [51]. The authors examined four groups to compare their electrochemical NRR capabilities. Among these metal phthalocyanines, the current efficiencies were ranked as follows: H (a free base phthalocyanine) > Ti, Fe > Pd > Co > Pt > Ni, In > Pb > Cu > Zn > Ga, Sn > Pb. Among them, the obtained Sn-based catalyst showed the best activity and stability. They concluded that the NRR activity depends strongly on the nature of the central metal ion of the metal phthalocyanine. The authors proposed that metal and metal oxides were the main catalysts for electrochemical formation of NH_3. Nonetheless, the underlying mechanism of these catalysts for improved NH_3 production was still unclear. Unexpectedly, the Sn(II) phthalocyanine catalysts were reevaluated in the same system by Symes et al. The authors claimed that the apparent NH_3 yield could be attributed to contaminants or electro-decomposition of these complexes [52].

The pioneering studies concluded that organic-coordinating ligand-introduced catalysts exhibited

promising NRR activities. Encouraged by this, the optimized NRR selectivity containing titanocene dichloride $((\eta^5\text{-}C_5H_5)_2TiCl_2$, commonly abbreviated as $CP_2TiCl_2)$ in 1.0 M LiCl aqueous electrolytes under ambient conditions was achieved by Yoon et al. [53]. The authors concluded that various proton sources and the nitrogen-transfer rate determine the resulting NRR selectivity. They suggested that Cp_2TiCl_2 remarkably lowers the activation barrier for N_2 dissociation, thereby promoting the NRR performance.

2.3　Ru catalyst

Previous studies have indicated that many stepped metals were structure-sensitive for the NH_3 formation reaction by enhancing the binding strength of N_2 molecules [35]. NH_3 synthesis via stepped surface science was investigated by Chorkendorff et al. in 2006 [54]. The authors found that the stepped surface contained active sites for N_2 dissociation. Similar defect-engineering and facet-orientation on metal-based catalysts are effective strategies to enhance N_2 adsorption on these active sites, thus reducing the energy barrier of N_2 dissociation [3].

For instance, metallic Ru has been studied for its potential for NH_3 formation [54, 55]. In 2000, Dahl, Chorkendorff, and coworkers used DFT to study the stepped surface of Ru [56], which was beneficial for low-barrier nitrogen dissociation and a more reactive NH_3 synthesis process than that provided by the Au-passivated Ru surface. In the same year, Kordali et al. developed a Ru/C catalyst for NH_3 production [21]. At −1.10 V vs. Ag/AgCl and 20 °C, the rate of NH_3 synthesis was 0.21 μg·h^{-1}·cm^{-2}. When the temperature was increased to 90 °C, the NH_3 production rate increased by approximately 4 times. The authors concluded that different planes of Ru were correlated to the number of active catalyst sites and the NRR reaction rate. Wessling et al. tested the NH_3 synthesis activity by electroplating Rh and Ru on Ti felts [46]. The Ru/Ti catalyst presented a higher density of defects in the obtained coatings and a stronger affinity of electrons than Rh/Ti, thereby contributing to its lower overpotential and higher NRR activity. Similarly, several other metallic catalysts, including Fe [57] and Pd [47], also afford favored NH_3 production, whose under- coordinated stepped surface functioned

as active sites to catalyze N_2 electrolysis.

2.4　Au catalyst

Typical research on the artificial NRR in a 0.1 M KOH solution was studied by Yan's group [27]. In this work, the authors successfully grew tetrahexahedral gold nanorods (THH Au NRs) with high index facets for a superior NRR performance using a seeded growth method. Figure 3(a) shows that the NRR test was conducted in the reaction cell under mild conditions. The resulting THH Au NRs were enclosed by stepped (730) facets (Figs. 3(b) and 3(c)). The as-obtained (730) facet, composed of (210) and (310) sub-facets (Fig. 3(d)), provided the as-prepared catalyst with a comparable electrical NRR activity (NH_3: 1.648 μg·h^{-1}·cm^{-2}, N_2H_4·H_2O: 0.102 μg·h^{-1}·cm^{-2}) at −0.2 V vs. RHE (reversible hydrogen electrode; Fig. 3(e)). Their electrocatalytic results show that increasing the number of exposed active sites benefits the NRR reaction. DFT calculations further confirmed that the unsaturated Au stepped facets function as the NRR active sites toward the cleavage of N≡N, thus forming chemisorbed Au-N bonds (Fig. 3(f)). The DFT results revealed that N atoms were more prone to being adsorbed than protons on the THH Au NRs.

2.5　Mo catalyst

Besides Ru and Au, similar findings of the facet-oriented effect were investigated on the Mo metal surface [58]. Inspired by a natural enzyme, nitrogenase, Wang et al. examined four types of Mo-based catalysts by varying the electro-deposition conditions, resulting in (110)- and (210)-oriented nanoparticle-clustered Mo. The (110)-oriented Mo nanoparticles show more preference for NH_3 production than the commercial Mo-foil and (210)-oriented Mo nanoparticles. The reason for the enhanced NRR properties is that the Mo (110) plane adsorbs N atoms more strongly than H atoms because of the lower adsorption energy of N (−1.1 eV) than that of H (−0.7 eV) [35]. Furthermore, the authors found that the nanosized structure could endow the catalytic surface with a high concentration of step sites. Owing to the synergistic effect between these active sites and the (110)-orientation, the Mo-based catalyst presented an NH_3 yield of 1.89 μg·h^{-1}·cm^{-2} and an FE of 0.72% at a lower overpotential of 0.14 V vs. RHE.
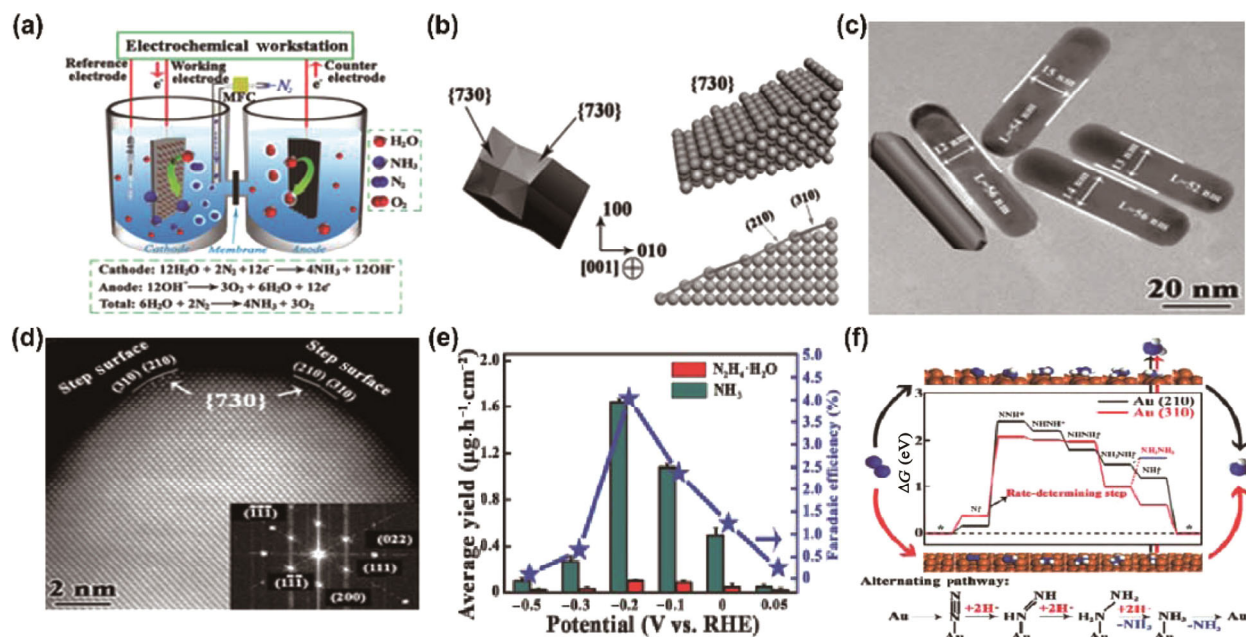
Figure 3 Electrocatalytic NRR on THH Au NRs. (a) Schematic for electrocatalytic NRR (MFC is the mass flow controller; the membrane is Nafion 211). (b) Geometric models of the Au THH NR and exposed (730) facet. The (730) facet is composed of (210) and (310) sub-facets on the Au NRs. (c) Transmission electron microscopy (TEM) image of Au THH NRs with diameter: 12–15 nm, length: 52–56 nm, and aspect ratio: 4 ± 0.5. (d) Spherical aberration-corrected TEM image of the Au THH NR with stepped sub-facets; the inset in (d) is the fast Fourier transform pattern of the indicated region. Reproduced with permission from Ref. [27], © WILEY-VCH 2017. (e) Yield rates of ammonia (cyan curve), hydrazine hydrate (red curve), and FEs (blue curve) at each given potential. (f) Free energy diagram and alternating hydriding pathway for NRR on Au (210) and Au (310) at equilibrium potential. Reproduced with permission from Ref. [27], © WILEY-VCH 2017.

3 Metal oxide-derived catalysts

3.1 Fe$_2$O$_3$ catalyst

In addition to the metal-based catalysts that are studied for electrochemical NH$_3$ generation from N$_2$ and H$_2$O, the capabilities of metal oxides for N$_2$ fixation have also been investigated [59]. Fe$_2$O$_3$ and its derivatives have been studied to reduce the side HER activity. For instance, theoretical insights on NH$_3$ synthesis from N$_2$ and steam electrolysis using a nano-Fe$_2$O$_3$ catalyst were explored by Nguyen et al. [36]. Considering the aforementioned Ru (0001) examples, similar phenomena were also reported at the under-coordinated Fe active sites on the hematite (0001) surfaces for the electrochemical reduction of N$_2$ to NH$_3$. These under-coordinated Fe sites show a relatively low electronegativity and are available to bind the N$_x$H$_y$ intermediates. An applied bias was still needed to reduce the proton transfer processes, and thus inhibit HER side effects.

In 2017, Centi et al. employed a hybrid Fe$_2$O$_3$-CNT (carbon nanotube) electrocatalyst for the NRR using water as a hydrogen source [34]. An electrochemical cell with a gas diffusion layer (GDL) electrode was used, as shown in Fig. 4(a). One half-cell was operated with a continuous N$_2$ flow and the other counter cell contained a diluted aqueous KHCO$_3$ solution, providing the protons and electrons for the synthesis of NH$_3$. In the gas-phase-type electrocatalytic flow half-cell, the Fe$_2$O$_3$-CNT electrocatalyst presented about three–four times higher NRR rates (0.22 μg·h^{-1}·cm^{-2}) than those of the o-CNT or nano-Fe$_2$O$_3$ samples (Fig. 4(b)). In this regard, the authors verified that the H$_2$ generation *in situ* had almost no effect on the rate of NH$_3$ formation, and suggested that the specific interface between Fe nanoparticles and CNTs serves as the active sites to dissociate N$_2$.

In the same year, Kong et al. also reported the electrochemical NRR at a low temperature and in aqueous solutions using a nanosized γ-Fe$_2$O$_3$ electrocatalyst [60]. An anion-exchange membrane electrode assembly was incorporated (Fig. 4(c)). The authors showed that the main side HER is suppressed under the deliberately
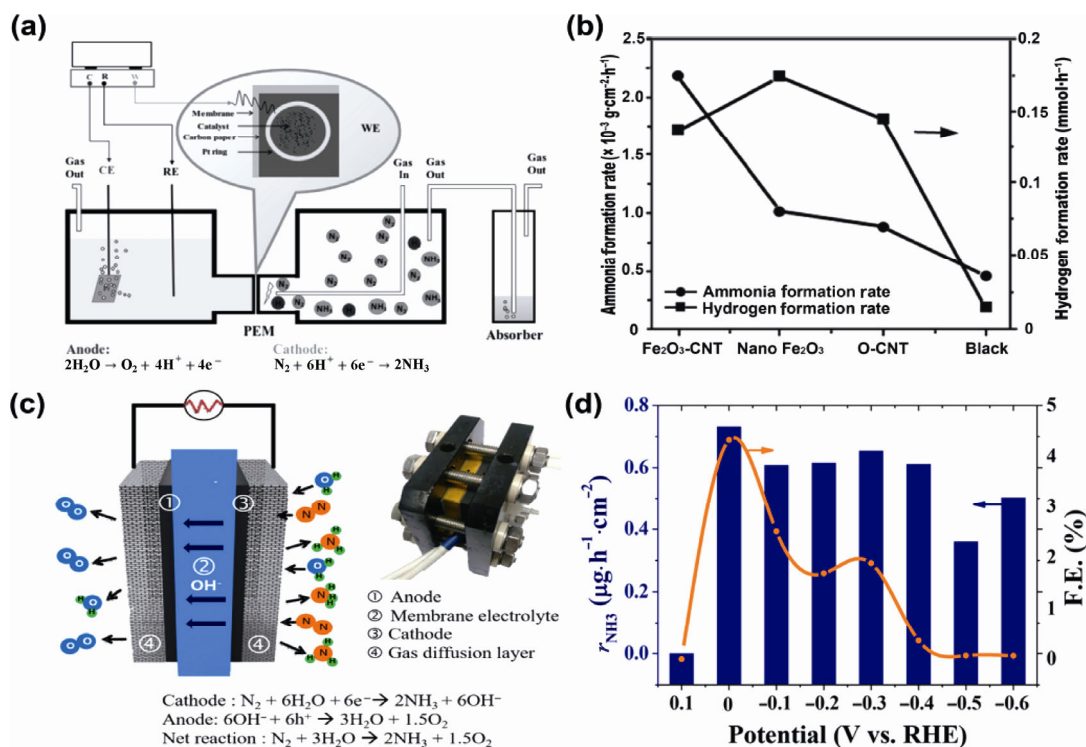
Figure 4 (a) Schematic view of the electrocatalytic flow reactor for NH_3 synthesis, with the cathode cell operating under electrolyte-less conditions (gas phase). (b) Faraday efficiency values of NH_3 formation and H_2 evolution under different applied voltages. Reproduced with permission from Ref. [34], © WILEY-VCH 2017. (c) Schematic of electrochemical synthesis of NH_3 in an anion-exchange-membrane-based electrolyzer, and photographic image of the actual inserted device. (d) NH_3 formation reaction rate (left y-axis) and faradaic efficiency (right y-axis) determined by chronoamperometry. Reproduced with permission from Ref. [60], © American Chemical Society 2017.

designed basic condition, and the NH_3 formation efficiency is pH-dependent on the catalyst surface. The resulting average NH_3 yield and FE values are displayed in Fig. 4(d). Although the weight- and area-normalized NRR performance of γ-Fe_2O_3 were reduced, surprisingly, the maximum FE of 1.9% and NH_3 formation rate of 43 nmol·h^{-1}·cm^{-2}$_{geo}$ were tested at a lower potential of 0.0 V vs. RHE. By comparing the NRR test results from the membrane electrode and disk electrode, the authors revealed that both the increased catalyst utilization and higher pH values contribute to the improved NRR activities of the γ-Fe_2O_3 catalyst. Distinct from the DFT analysis on nano-Fe_2O_3 discussed above, the researchers obtained a different conclusion that the NRR selectivity decreased with a more negative bias because of competition from the HER.

3.2 Other metal oxide catalysts

Besides nano-Fe_2O_3 and its derivatives, several studies have examined other oxide catalysts [61]. In 1990,

Furuya et al. studied the NRR efficiency of seven metal oxides and hybrid catalysts, and showed that the activity trend follows: PbO-TiO_2 > Sb-SnO_2 > ZnO > Sn-In_2O_3 > SnO_2 > Fe_2O_3 > TiO_2 [62]. They demonstrated that the current efficiency depends on the nature of the metal, such as its oxidation state. Skúlason et al. also carried out DFT calculations on the (110) facet of eleven metal oxides in the rutile structure, including NbO_2, RuO_2, RhO_2, TaO_2, ReO_2, TiO_2, OsO_2, MnO_2, CrO_2, IrO_2, and PtO_2, to investigate their facet dependency [61]. They calculated the relative stability between the oxide crystal facet and the mediated adsorbates, function to free energy, and catalytic activity. The authors predicted that among those oxides, ReO_2 and TaO_2 favor NNH adsorption rather than hydrogen adsorption, thus inhibiting the HER rate and providing higher NRR activities.

In addition, some studies used multi-oxides for the NRR [63]. Taking Bi_2MoO_6 as an example, Dong et al. reported a Bi_2MoO_6-based catalyst with unsaturated

Mo atoms that functioned as active sites to achieve chemical adsorption, activation, and N_2 reduction [13]. With the aim of blocking the under-coordinated Bi_2MoO_6-based catalysts, the addition of different concentrations of polyvinylpyrrolidone confirmed that the special Mo area is the N_2 dissociation active center.

3.3 Metal/metal oxide composite catalysts

Aside from the oxide catalysts above, a Au/TiO_2 composite catalyst for enhancing the selectivity of the NRR was recently reported by Yan's group [39]. The TA (tannic acid) surfactant molecules act as both the reducing and immobilizing agents; thus, the obtained TA-reduced materials show a high dispersion of sub-nanometer Au clusters, with an average size of ~ 0.5 nm (Figs. 5(a) and 5(b)). Similar to the nanosized metal-based catalysts, it was suggested that a high density of low-coordination sites on sub-nanometer particles were responsible for the enhanced NRR activity. In addition, the high dispersion of Au active centers anchored on the TiO_2 support was attributed to the strong chemical bonding between the sub-nanometer Au clusters and lattice oxygen of TiO_2. Figure 5(c) shows that the NRR rate increased as the applied

negative potential increased, but the best performance was obtained at −0.2 V vs. RHE, with an NH_3 yield of 21.4 $\mu g \cdot h^{-1} \cdot mg^{-1}_{cat.}$ and FE of 8.11% [39]. The authors explained that the formation of Au-O-Ti improved the Au metal stability, and accelerated more electron transfers from the Au clusters to the TiO_2 substrate, thus achieving a higher NRR selectivity. A similar effect was reported for other metal-support interactions [64, 65]. In this context, the authors obtained several Au/TiO_2 hybrid catalysts using three different reducing methods: TA-reduction, $NaBH_4$-reduction, and photoreduction. Among them, the best catalyst for an efficient NRR was the TA-reduced Au/TiO_2 electrocatalyst (Fig. 5(d)). The authors concluded that the small size effect of sub-nanometer Au on the TiO_2 substrate may be the key factor for an enhanced NRR performance.

Following the previous study, the same group constructed a Au/CeO_x-RGO (reduced graphite oxide) ternary hybrid system for the NRR using a facile co-reduction method [32]. Figure 6(a) demonstrates that the Au nanoparticles (average size of ~ 5 nm) were well dispersed on the surface of CeO_x-RGO. As for the Au/TiO_2 catalyst, the best electrochemical NRR result was obtained at −0.2 V vs. RHE (Fig. 6(b)). The
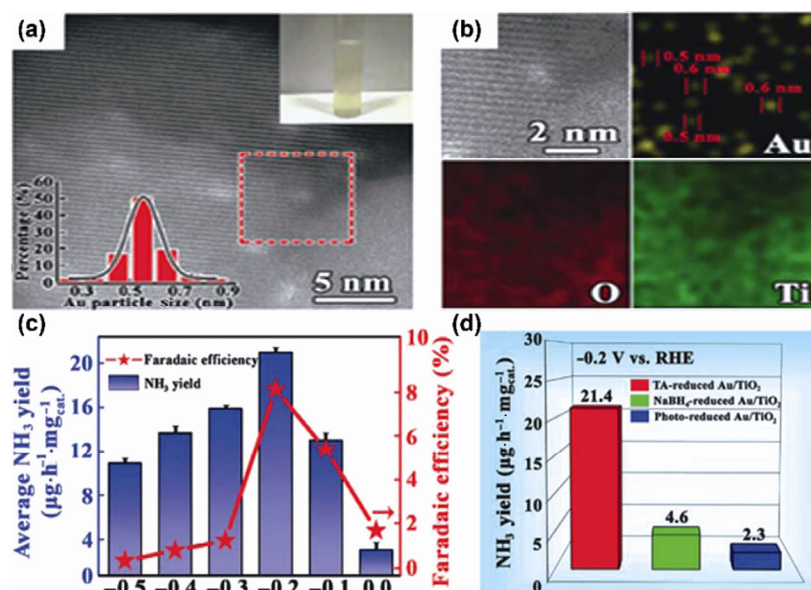
Figure 5 (a) Representative spherical aberration-corrected high-angle annular dark-field/scanning transmission electron microscopy (STEM) image of TA-reduced Au/TiO_2 (the upper inset is a photograph of TA-reduced Au/TiO_2 suspended in water, and the lower inset is the particle size distribution of Au). (b) STEM/energy-dispersive X-ray spectroscopy elemental mapping (Au, Ti, and O elements) of TA-reduced Au/TiO_2 (the selected area is framed in (c), and the Au cluster size is ~ 0.5 nm). (c) Yield rate of NH_3 (blue) and Faradaic efficiency (red) at each given potential. (d) Yield rate of NH_3 with different catalysts at −0.2 V vs. RHE at room temperature and ambient pressure. Reproduced with permission from Ref. [39], © WILEY-VCH 2017.
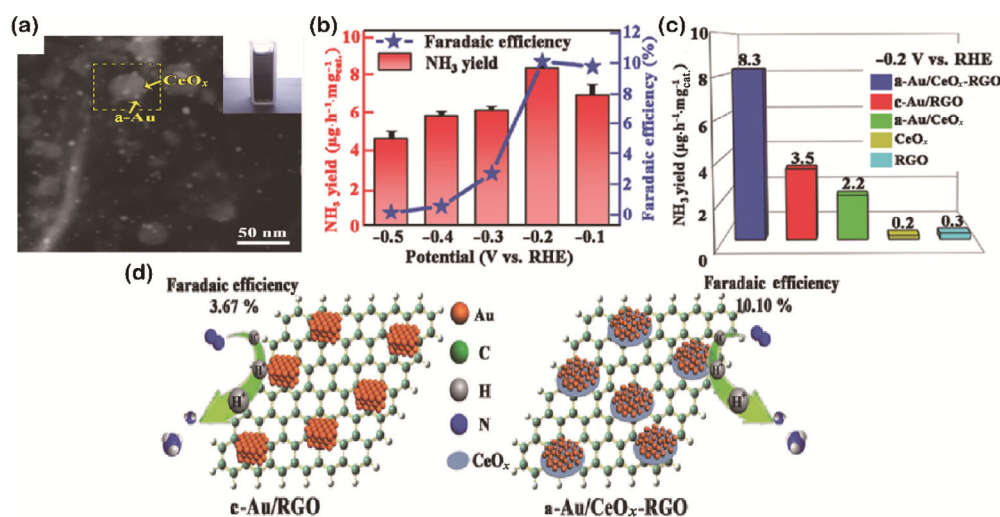
Figure 6 (a) Representative STEM image of a-Au/CeO$_x$-RGO; the inset is a photograph of a-Au/CeO$_x$-RGO suspended in water. (b) Yield of NH$_3$ (red) and faradaic efficiency (blue) at each given potential. (c) Yield of NH$_3$ with different catalysts at −0.2 V vs. RHE at room temperature and atmospheric pressure. (d) Schematic illustration for the electrochemical NRR by a-Au/CeO$_x$-RGO and c-Au/RGO catalysts under ambient conditions. Reproduced with permission from Ref. [32], © WILEY-VCH 2017.

experiments for amorphous Au on CeO$_x$ with its crystalline counterpart on RGO (Fig. 6(c)) indicated that the presence of CeO$_x$ was crucial for transforming crystallized Au to amorphous Au. The scheme in Fig. 6(d) displays a clear distinction in the FE between CeO$_x$-RGO and a-Au/CeO$_x$-RGO (a-Au represents amorphous Au). Hence, the researchers concluded that Au nanoparticles were in an amorphous state because of the existence of CeO$_x$ and possessed a higher concentration of unsaturated coordination sites for excellent NRR results. These studies from Yan's group indicate that the interface interaction between the metal and oxide support contributes to high dispersions, small sizes, or amorphous states in the metal active centers [66]. The underlying reasons may be correlated to the lattice strain effect [3, 67], or an activation barrier to prevent the metal atoms from diffusing together and catalyst from sintering [68].

4   Other hybrid catalysts

4.1   Polymer catalysts

Indeed, another early report of the electrochemical NRR at a mild temperature and pressure in an aqueous system was that using metal phthalocyanines by Furuya et al. in 1989 [51], as discussed previously. This work aimed to investigate the effect of the metal center of metal-phthalocyanines for the NRR efficiency, but the

role of phthalocyanines was not investigated in detail. Recently, deliberately designing Li$^+$ incorporation is a promising strategy to achieve excellent NRR properties. Taking the Li$^+$-intercalated polymer system as an example, Wang et al. successfully explored a Li$^+$-inserted PEBCD (poly(N-ethyl-benzene-1,2,4,5-tetracarboxylic diimide)) hybrid as an NRR catalyst [26], aiming to suppress the side HER. Previous research revealed that oxygen atoms in the polymer catalysts are beneficial for the HER. In this regard, our group developed a PNFE (polyimide) nanosheet array on CNTs (designated as PNFE/CNT), which served as a current collector, to afford a passivated HER activity and capability for Li$^+$ storage [69]. Predictably, Li-incorporation blocked the corresponding surface sites, resulting in a high potential energy barrier for the side HER. In this research, the NRR test was conducted in the reaction cell under mild conditions (Fig. 7(a)). As shown in Fig. 7(b), the final amorphous PEBCD/C catalyst was prepared by a simple *in situ* polycondensation on the carbon cloth fibers. The inserted element mapping results indicate that the distribution of C and O elements are uniform on amorphous PEBCD. The best FE (Fig. 7(c)) and NH$_3$ yield rate (Fig. 7(d)) (1.58 μg·h^{-1}·cm^{-2} and 2.85%, respectively) were obtained by varying the negative potential. They explained that H$_2$ slowing contributes to the enhanced NRR selectivity because Li$^+$ can associate with the completely exposed oxygen
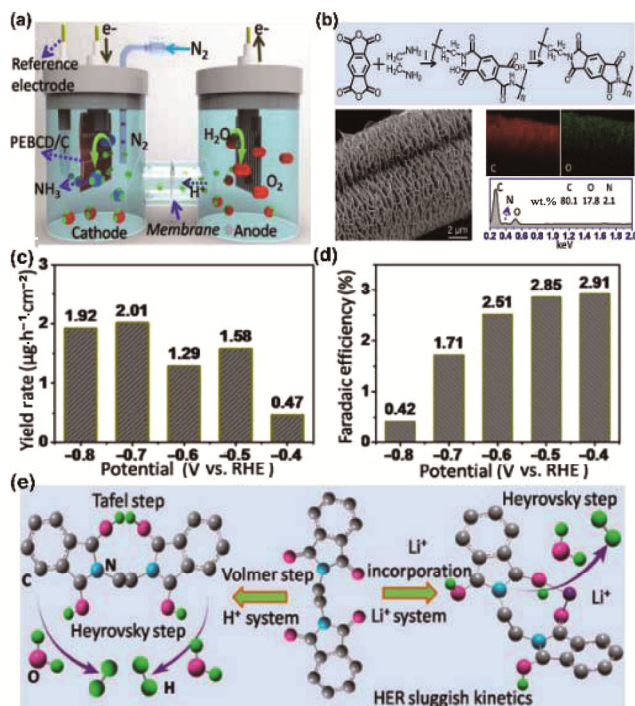
Figure 7 NRR behavior of PEBCD/C. (a) Schematic reaction cell for NRR (inset: Element mapping and energy dispersive spectroscopy). (b) Faradaic efficiency and (c) NH_3 yield rate at various potentials and 25 °C. (d) Schematic illustration of Li^+ association with O sites. Reproduced with permission from Ref. [26], © American Chemical Society 2017. (e) Schematic illustration of Li-ion association with O sites. Reproduced with permission from Ref. [26], © American Chemical Society 2017.

sites in PEBCD (Fig. 7(e)).

4.2 Other hybrid catalysts

Other hybrid catalysts, such as non-metal catalysts [37], metal nitrides [70], metal carbides [71], and metal-organic frameworks [72], have been reported for NH_3 synthesis. In 1990, Furuya et al. also investigated the NRR efficiency of a series of metal sulfides and SiC, TiB, and ZnSe; among them, the best electrochemical NRR performance was observed on the ZnSe catalyst [62]. They found that metal sulfides are better than their corresponding oxides. In 2016, DFT studies on thirteen different transition metal nitrides for electrocatalytic reduction of N_2 were carried out by Skúlason et al. [73]. They demonstrated the available results on VN, ZrN, NbN, and CrN, which favor the NRR instead of the competing HER from air and water at a low applied bias (Fig. 8(a)). More importantly, a deeper understanding of the correlations on the migration and regeneration

of the N vacancy of the nitride catalysts, and their relationship to the sustainable NRR catalytic cycle, will help to design promising NRR catalysts (Fig. 8(b)) [31]. Single transition metal atoms (Sc to Zn, Mo, Ru, Rh, Pd, and Ag) supported on a defective BN monolayer with a boron monovacancy served as a N_2 fixation electrocatalyst, as reported by Chen et al. [74]. Among them, the Mo-embedded BN monolayer with a B-vacancy presented the highest catalytic activity because of the high spin polarization and selective stabilization of the intermediates (N_2H^* and NH_2^* species).

5 Effect of various electrolytes

In addition to the metal surface structure, there are some reports on the effect of various electrolytes for metal-based catalysts for NH_3 formation. In 1989, Furuya et al. claimed that potassium salts were better electrolytes than sodium salts in terms of the current efficiency and stability of NRR catalysts [50]. However, the reasons for the different current efficiencies and stabilities were not discussed. In 2010, polypyrrole was used as a polymer catalyst for low-overpotential fixation of nitrogen in an aqueous solution containing 0.1 M Li_2SO_4 and 0.03 M H^+, as reported by Fatih Köleli et al. [75]. The authors explored the reverse effect of the electrolyte on an aqueous milieu in terms of NH_3 production, and found that the NRR activity follows a sequence: $Li^+ > Na^+ > K^+ > Cs^+$. Li^+ ions were suggested to have a larger hydration radius, thus leaving the metal surface more available. The authors proposed a different electrochemical hydrogenation mechanism for the polymer-coated electrodes: Successive addition of H_{ad} species to N_2 molecules [27].

Recently, Han et al. studied NH_3 electrosynthesis in a mixture of water and 2-propanol under ambient conditions using porous Ni as an anode catalyst [76]. The existence of 2-propanol in the electrolyte increased the solubility of N_2 and diminished the competitive hydrogen reduction reaction (HER). Thus, in the NRR test, the porous Ni-based catalyst can present a higher NRR performance in the special electrolyte than in the absence of 2-propanol. Considering the instability of the polymer in a reducing environment, another similar study based on ethylenediamine, which served as a stable cathodic solvent, was developed by the same researchers [77]. Additionally, Centi et al. conducted
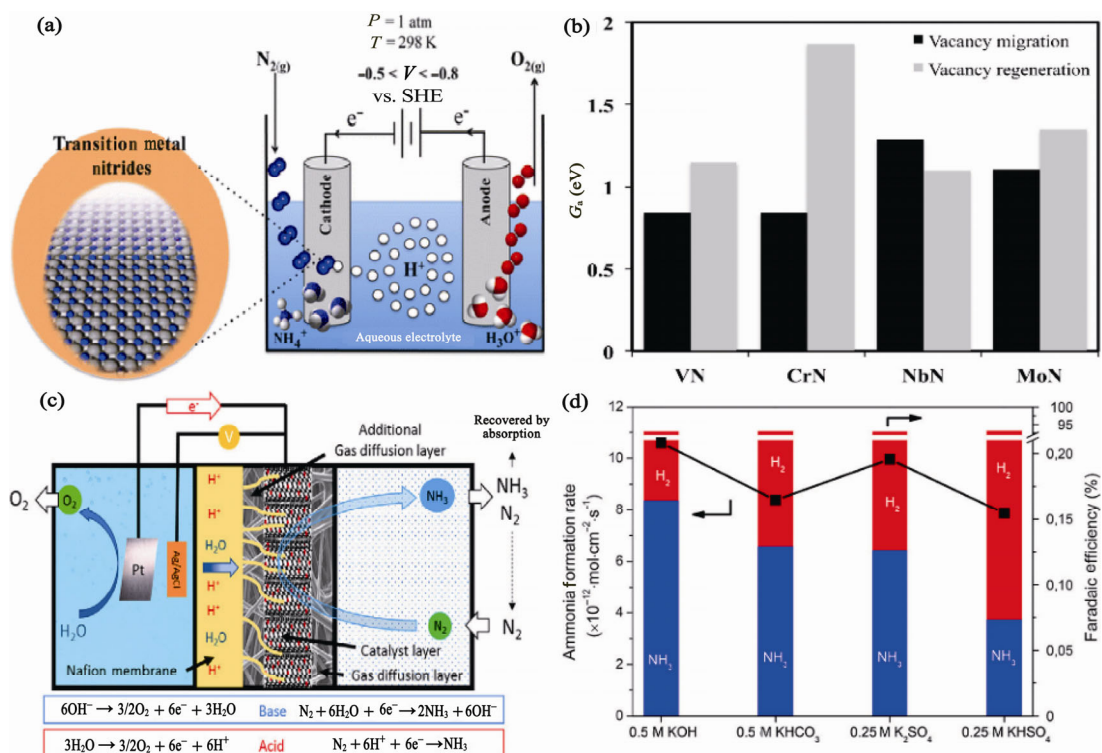
Figure 8 (a) Schematic reaction cell for the NRR by transition metal nitrides. Reproduced with permission from Ref. [31], © Elsevier B.V. 2017. (b) Calculated activation free energies (G_a) for regenerating the catalyst by N_2 dissociation to replenish the N-vacancy compared with the activation free energies of vacancy migration into the bulk (migration of N atoms from the bulk toward the surface). Reproduced with permission from Ref. [73], © American Chemical Society 2017. (c) Schematic view of the improved design in a three-phase reactor for electrochemical NH_3 synthesis. (d) Average NH_3 formation rate and faradaic efficiency of the electrocatalyst using different electrolytes. Reproduced with permission from Ref. [33], © American Chemical Society 2017.

a series of investigations on the effect of the electrolyte (e.g., type, pH, and concentration) on the NRR activity by employing hybrid Fe_2O_3-CNTs as the electrocatalyst [33]. Compared to the previous study, they prevented the possible NH_3 diffusion into the anode cell by inserting a GDL, as shown in Fig. 8(c). The operando X-ray absorption fine structure analysis indicated that Fe_2O_3 reduction promoted the side HER. In addition to the basic electrolyte, neutral and acidic electrolytes were also employed to evaluate the pH effect on NH_3 formation from H_2O and N_2 based on kinetic considerations (Fig. 8(d)). The authors concluded that the N_2 conversion rate only depends on the proton concentration under acidic conditions, but it is determined by both proton concentration and water transport in basic electrolytes.

6 Li-N$_2$ batteries

Interestingly, a new pathway for N_2 fixation using a

special Li-N$_2$ battery was successfully designed by Zhang et al. [78]. Based on the reversible reaction of $6Li + N_2 \rightarrow 2Li_3N$, the Li-N$_2$ battery supplies electric energy for the reversible N_2/Li_3N cycle, as shown in Fig. 9(a). Moreover, Fig. 9(b) clearly depicts the gradually darkening color of the solution, revealing the accumulation of Li_3N (A–C inserted). However, the return to a transparent solution demonstrated the decomposition of Li_3N (D–F inserted). As a result, the Li-N$_2$ battery achieved a high FE of 59% and provided a unique strategy for efficient N_2 reduction. Correspondingly, the authors further investigated the Li-N$_2$ battery reaction processes using various *ex situ* characteristics, as displayed in Figs. 9(c)–9(e). Some particles had deposited on the smooth carbon cloth after N_2 fixation, which is similar to the results from the colorimetric analysis, whereas the particles subsequently disappeared as charging proceeded. By enabling such a reversible N_2/Li_3N cycle approach, this Li-N$_2$ battery suggests a new means for nitrogen-fixable and energy-storage systems.
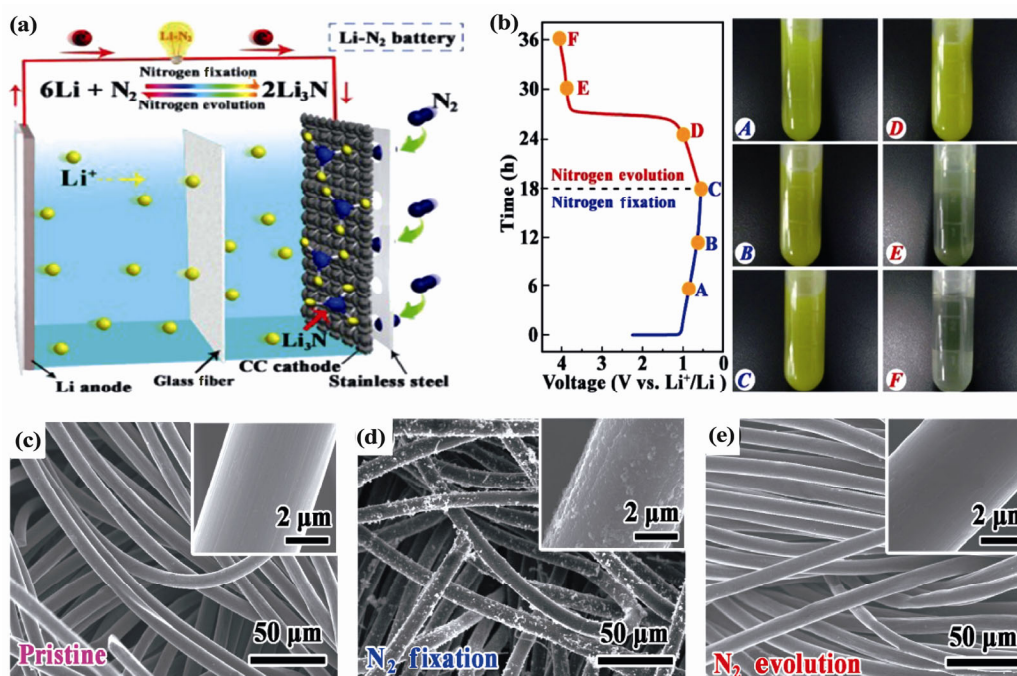
Figure 9 (a) Structure of a Li-N_2 battery with a Li foil anode, ether-based electrolyte, and carbon cloth (CC) cathode. (b) Colorimetric analysis of the electrochemical nitrogen fixation and evolution processes. (c)–(e) Scanning electron microscopy images of the CC cathode at different electrochemical conditions. Reproduced with permission from Ref. [78], © Elsevier Inc. 2017.

To briefly conclude, we representatively summarized the recent progress in the electrochemical NRR from ambient temperatures and pressures, plus the roles of different types of aqueous electrolytes that should be considered to reduce the competing HER (Table 1).

7 Conclusions and prospects

Modern society cannot be sustained without the conversion of NH_3 from inert N_2. With the continuous increases in the human population and carbon emissions, developing new sustainable and economical approaches for NH_3 synthesis to support growing global demands is increasingly imminent. The electrocatalytic NRR at ambient temperatures is among the most promising means, with potentials of low carbon emission, reduced energy consumption, and easy implementation, even in many underdeveloped areas. The successful realization of an efficient and selective NRR strongly relies on two major research directions. Advances in design concepts and synthetic methods, such as tuning crystal facets and defects, controlling atomic doping and d-band center tuning, and coordinating ligand-introduction and structure vacancies, can lead to new NRR electrocatalysts. However,

the water reduction HER, which is the major side reaction that competes for protons and electrons, must be substantially suppressed, e.g., using different pH solutions or electrolytes, controlled release of protons, and blocking the active sites of HER using a Li^+ electrolyte or Li^+ ion insertion.

Despite the substantial developments so far, several fundamental challenges need to be addressed to realize electrocatalytic nitrogen reduction at a practical level and possibly replace the current Haber-Bosch process. First, from a thermodynamic point of view, NRR pathways are possible at ambient temperatures. However, the reaction rates and turnover frequencies reported to date have been too low, and a larger overpotential is required. The NH_3 production rates from most reports are in the range of a microgram per hour per square centimeter of catalyst, which is far below the requirement for practical industry applications.

Second, the selectivities of almost all the current NRR electrocatalyst are still at the very low end (FE < 10%, and even below 1% most of the time), which are dominated by water reduction (HER) that shuttles electrons and protons to form hydrogen. Assuming all the electricity for the NRR is from solar-to-electricity

Table 1 Summary of the representative reports on electrochemical N_2 reduction in aqueous solutions at a low temperature and ambient pressure

Temperature	Catalyst	Electrolyte	Yield	FE (%)	Potential	Ref.
25 °C	Au nanorod	0.1 M KOH	1.648 µg·h^{-1}·cm^{-2} (NH_3) 0.102 µg·h^{-1}·cm^{-2} (N_2H_4·H_2O)	4.02	−0.2 V vs. RHE	[27]
20 °C	Au/TiO$_2$	0.1M HCl	21.4 µg·h^{-1}·mg^{-1}	8.11	−0.2 V vs. RHE	[38]
25 °C	a-Au/CeO$_x$-RGO	0.1 M HCl	8.3 µg·h^{-1}·mg^{-1}	10.1	−0.2 V vs. RHE	[32]
20 °C	Fe$_2$O$_3$-CNT	0.1 M KHCO$_3$	0.22 µg·h^{-1}·cm^{-2}	0.15	−1.0 V vs. Ag/AgCl	[34]
25 °C	Fe$_2$O$_3$-CNT	0.5 M KOH	0.41 µg·h^{-1}·cm^{-2}	0.03	−1.0 V vs. Ag/AgCl	[33]
25 °C	PEBCD^a/C	0.5 M Li$_2$SO$_4$	1.58 µg·h^{-1}·cm^{-2}	2.85	−0.5 V vs. RHE	[26]
25 °C	(110)-oriented Mo	Aqueous solutions	1.89 µg·h^{-1}·cm^{-2}	0.72	−0.49 V vs. RHE	[58]
20 °C	Ru/C	2 M KOH	0.21 µg·h^{-1}·cm^{-2}	0.28	−1.1 V vs. Ag/AgCl	[21]
30 °C	Ru/Ti	0.5 M H$_2$SO$_4$	7.31 µg·h^{-1}·cm^{-2}	N/A	N/A	[46]
25 °C	ZnSe	1.0 M KOH	6.39×10^{-9} mol·s^{-1}·cm^{-2}	1.3	−1.0 V vs. RHE	[62]
25 °C	Ni	0.1 M LiCl/EDA^b	3.58×10^{-11} mol·s^{-1}·cm^{-2}	17.2	1.8 V (N/A)	[77]
Room temperature	30 wt.% Pt/C	H$_2$O	1.14×10^{-9} mol·s^{-1}·cm^{-2}	0.52	−1.6V (N/A)	[79]
Ambient temperature	Porous Ni	Mixture of water/2-propanol	1.54×10^{-11} mol·s^{-1}·cm^{-2}	0.89	N/A	[76]
25 °C	Fe-phthalocyanine	1.0 M KOH	5.57×10^{-10} mol·s^{-1}·cm^{-2}	0.33	N/A	[50]
25 °C	PAn^c film	0.1 M LiClO$_4$ in ethanol	1.5×10^{-10} mol·s^{-1}· m^{-2}	7	−0.12 vs. NHE	[80]
50 °C	Pt, Fe, Ni, FeNi	H$_2$O	1.33×10^{-12}–3.80×10^{-12} mol·s^{-1}·cm^{-2}	1.1–41	−1.2 V (N/A)	[59]
80 °C	Pt/C	0.1 M Li$_2$SO$_4$	9.37×10^{-10} mol·s^{-1}·cm^{-2}	0.83	−1.2 vs. Ag/AgCl	[81]
90 °C	MOF(Fe)	H$_2$O	2.12×10^{-9} mol·s^{-1}·cm^{-2}	1.43	−1.2 vs. Ag/AgCl	[72]

^{a}PEBCD, poly(N-ethyl-benzene-1,2,4,5-tetracarboxylic diimide). ^{b}EDA, ethylenediamine. ^{c}PAn, polyaniline.

conversion, the low selectivity and reaction rates will require a large photovoltaic panel (approximately 5% of the fields that would need fertilizers) [1], which is prohibitively expensive and impractical. On the other hand, enzymes from plants or microorganisms have better selectivities toward NH_3 production [82–84], but they are fragile and provide few turnovers. Thereafter, the development of new catalyst systems with much better conversion yields and selectivities are surely valuable.

Moreover, considering the universal existence of water molecules and the low solubility of nitrogen in aqueous solutions, this deficiency inevitably lowers the encountering frequency of N_2 molecules compared to H_2O at the electrocatalyst surface. Even for basic solutions, there are a significant number of protons from water. Theoretical calculations have suggested that if the access of protons onto an electrocatalyst surface can be significantly limited, the adsorption rate of N_2 can surpass that of H^+, which can be ready for

the NRR when protons and electrons are subsequently provided [1]. Thus, exploring mechanisms for efficient delivery of N_2 molecules that limit the proton availability is also highly important. Applying gas delivery device structures, such as a GDL, can certainly enhance the mass transfer of N_2 toward the catalyst surface. Low proton conditions may be thermodynamically realized using an aprotic or extremely alkaline solvent. Alternatively, from a kinetic point of view, the catalyst can be protected by a hydrophobic surrounding layer that allows N_2 to pass but significantly hinders proton transfer, or by sterically large proton donor molecules with poor proton transfer kinetics [85].

In conclusion, the continuous development and eventual realization of efficient approaches for electrochemical reduction of N_2 to NH_3 under ambient and convenient conditions shows strong potentials for producing fertilizers and nitrogen-containing products, while significantly reducing global energy costs and carbon emissions [86, 87]. Coupling with renewable energy sources, this

nitrogen fixation scenario of the electrocatalytic NRR may lead to a dramatic change in the present infrastructures of the Haber-Bosch process toward more convenient and available processes throughout the world.

Acknowledgements

References

[1] Singh, A. R.; Rohr, B. A.; Schwalbe, J. A.; Cargnello, M.; Chan, K.; Jaramillo, T. F.; Chorkendorff, I.; Nørskov, J. K. Electrochemical ammonia synthesis-The selectivity challenge. *ACS Catal.* **2017**, *7*, 706–709.

[2] Cui, B. C.; Zhang, J. H.; Liu, S. Z.; Liu, X. J.; Xiang, W.; Liu, L. F.; Xin, H. Y.; Lefler, M. J.; Licht, S. Electrochemical synthesis of ammonia directly from N_2 and water over iron-based catalysts supported on activated carbon. *Green Chem.* **2017**, *19*, 298–304.

[3] Schlögl, R. Catalytic synthesis of ammonia-A "never-ending story"? *Angew. Chem., Int. Ed.* **2003**, *42*, 2004–2008.

[4] Klerke, A.; Christensen, C. H.; Nørskov, J. K.; Vegge, T. Ammonia for hydrogen storage: Challenges and opportunities. *J. Mater. Chem.* **2008**, *18*, 2304–2310.

[5] Brown, K. A.; Harris, D. F.; Wilker, M. B.; Rasmussen, A.; Khadka, N.; Hamby, H.; Keable, S.; Dukovic, G.; Peters, J. W.; Seefeldt, L. C. et al. Light-driven dinitrogen reduction catalyzed by a CdS: Nitrogenase MoFe protein biohybrid. *Science* **2016**, *352*, 448–449.

[6] Service, R. F. New recipe produces ammonia from air, water, and sunlight. *Science* **2014**, *345*, 610.

[7] Rosca, V.; Duca, M.; de Groot, M. T.; Koper, M. T. M. Nitrogen cycle electrocatalysis. *Chem. Rev.* **2009**, *109*, 2209–2244.

[8] Licht, S.; Cui, B. C.; Wang, B. H.; Li, F. F.; Lau, J.; Liu, S. Z. Ammonia synthesis by N_2 and steam electrolysis in molten hydroxide suspensions of nanoscale Fe_2O_3. *Science* **2014**, *345*, 637–640.

[9] van Kessel, M. A. H. J.; Speth, D. R.; Albertsen, M.; Nielsen, P.

H.; Op den Camp, H. J. M.; Kartal, B.; Jetten, M. S. M.; Lücker, S. Complete nitrification by a single microorganism. *Nature* **2015**, *528*, 555–559.

[10] Shipman, M. A.; Symes, M. D. Recent progress towards the electrosynthesis of ammonia from sustainable resources. *Catal. Today* **2017**, *286*, 57–68.

[11] Mikkelsen, M.; Jørgensen, M.; Krebs, F. C. The teraton challenge. A review of fixation and transformation of carbon dioxide. *Energy Environ. Sci.* **2010**, *3*, 43–81.

[12] Galloway, J. N.; Cowling, E. B. Reactive nitrogen and the world: 200 years of change. *Ambio* **2002**, *31*, 64–71.

[13] Hao, Y. C.; Dong, X. L.; Zhai, S. R.; Ma, H. C.; Wang, X. Y.; Zhang, X. F. Hydrogenated bismuth molybdate nanoframe for efficient sunlight-driven nitrogen fixation from air. *Chem. Eur. J.* **2016**, *22*, 18722–18728.

[14] Burgess, B.; Wherland, S.; Newton, W.; Stiefel, E. I. Nitrogenase reactivity: Insight into the nitrogen-fixing process through hydrogen-inhibition and HD-forming reactions. *Biochemistry* **1981**, *20*, 5140–5146.

[15] Zhu, D.; Zhang, L. H.; Ruther, R. E.; Hamers, R. J. Photo-illuminated diamond as a solid-state source of solvated electrons in water for nitrogen reduction. *Nat. Mater.* **2013**, *12*, 836–841.

[16] Sun, S. M.; Li, X. M.; Wang, W. Z.; Zhang, L.; Sun, X. Photocatalytic robust solar energy reduction of dinitrogen to ammonia on ultrathin MoS_2. *Appl. Catal. B: Environ.* **2017**, *200*, 323–329.

[17] Li, X. M.; Wang, W. Z.; Jiang, D.; Sun, S. M.; Zhang, L.; Sun, X. Efficient solar-driven nitrogen fixation over carbon-tungstic-acid hybrids. *Chemistry* **2016**, *22*, 13819–13822.

[18] Sun, S. M.; An, Q.; Wang, W. Z.; Zhang, L.; Liu, J. J.; Goddard III, W. A. Efficient photocatalytic reduction of dinitrogen to ammonia on bismuth monoxide quantum dots. *J. Mater. Chem. A* **2017**, *5*, 201–209.

[19] Li, H.; Shang, J.; Ai, Z. H.; Zhang, L. Z. Efficient visible light nitrogen fixation with BiOBr nanosheets of oxygen vacancies on the exposed {001} facets. *J. Am. Chem. Soc.* **2015**, *137*, 6393–6399.

[20] Yandulov, D. V.; Schrock, R. R. Catalytic reduction of dinitrogen to ammonia at a single molybdenum center. *Science* **2003**, *301*, 76–78.

[21] Kordali, V.; Kyriacou, G.; Lambrou, C. Electrochemical synthesis of ammonia at atmospheric pressure and low temperature in a solid polymer electrolyte cell. *Chem. Commun.* **2000**, 1673–1674.

[22] Pappenfus, T. M.; Lee, K.; Thoma, L. M.; Dukart, C. R. Wind to ammonia: Electrochemical processes in room temperature Ionic liquids. *ECS Trans.* **2009**, *16*, 89–93.

[23] Lu, Y. F.; Li, J.; Tada, T.; Toda, Y.; Ueda, S.; Yokoyama, T.; Kitano, M.; Hosono, H. Water durable electride Y_5Si_3:

Electronic structure and catalytic activity for ammonia synthesis. *J. Am. Chem. Soc.* **2016**, *138*, 3970–3973.

[24] Kugler, K.; Ohs, B.; Scholz, M.; Wessling, M. Towards a carbon independent and CO_2-free electrochemical membrane process for NH_3 synthesis. *Phys. Chem. Chem. Phys.* **2014**, *16*, 6129–6138.

[25] Guo, X. H.; Zhu, Y. P.; Ma, T. Y. Lowering reaction temperature: Electrochemical ammonia synthesis by coupling various electrolytes and catalysts. *J. Energy Chem.* **2017**, *26*, 1107–1116.

[26] Chen, G. F.; Cao, X. R.; Wu, S. Q.; Zeng, X. Y.; Ding, L. X.; Zhu, M.; Wang, H. H. Ammonia electrosynthesis with high selectivity under ambient conditions via a Li^+ incorporation strategy. *J. Am. Chem. Soc.* **2017**, *139*, 9771–9774.

[27] Bao, D.; Zhang, Q.; Meng, F. L.; Zhong, H. X.; Shi, M. M.; Zhang, Y.; Yan, J. M.; Jiang, Q.; Zhang, X. B. Electrochemical reduction of N_2 under ambient conditions for artificial N_2 fixation and renewable energy storage using N_2/NH_3 cycle. *Adv. Mater.* **2017**, *29*, 1604799.

[28] Kyriakou, V.; Garagounis, I.; Vasileiou, E.; Vourros, A.; Stoukides, M. Progress in the electrochemical synthesis of ammonia. *Catal. Today* **2017**, *286*, 2–13.

[29] Kuang, M.; Zheng, G. F. Nanostructured bifunctional redox electrocatalysts. *Small* **2016**, *12*, 5656–5675.

[30] Li, J.; Zheng, G. F. One-dimensional earth-abundant nanomaterials for water-splitting electrocatalysts. *Adv. Sci.* **2017**, *4*, 1600380.

[31] Abghoui, Y.; Skúlason, E. Electrochemical synthesis of ammonia via Mars-van Krevelen mechanism on the (111) facets of group III–VII transition metal mononitrides. *Catal. Today* **2017**, *286*, 78–84.

[32] Li, S. J.; Bao, D.; Shi, M. M.; Wulan, B. R.; Yan, J. M.; Jiang, Q. Amorphizing of Au nanoparticles by CeO_x-RGO hybrid support towards highly efficient electrocatalyst for N_2 reduction under ambient conditions. *Adv. Mater.* **2017**, *29*, 1700001.

[33] Chen, S. M.; Perathoner, S.; Ampelli, C.; Mebrahtu, C.; Su, D. S.; Centi, G. Room-temperature electrocatalytic synthesis of NH_3 from H_2O and N_2 in a gas–liquid–solid three-phase reactor. *ACS Sustain. Chem. Eng.* **2017**, *5*, 7393–7400.

[34] Chen, S. M.; Perathoner, S.; Ampelli, C.; Mebrahtu, C.; Su, D. S.; Centi, G. Electrocatalytic synthesis of ammonia at room temperature and atmospheric pressure from water and nitrogen on a carbon-nanotube-based electrocatalyst. *Angew. Chem., Int. Ed.* **2017**, *56*, 2699–2703.

[35] Skulason, E.; Bligaard, T.; Gudmundsdottir, S.; Studt, F.; Rossmeisl, J.; Abild-Pedersen, F.; Vegge, T.; Jónsson, H.; Nørskov, J. K. A theoretical evaluation of possible transition metal electro-catalysts for N_2 reduction. *Phys. Chem. Chem. Phys.* **2012**, *14*, 1235–1245.

[36] Nguyen, M. T.; Seriani, N.; Gebauer, R. Nitrogen electrochemically reduced to ammonia with hematite: Density-functional insights.

Phys. Chem. Chem. Phys. **2015**, *17*, 14317–14322.

[37] Kumar, C. V. S.; Subramanian, V. Can boron antisites of BNNTs be an efficient metal-free catalyst for nitrogen fixation? -A DFT investigation. *Phys. Chem. Chem. Phys.* **2017**, *19*, 15377–15387.

[38] Shi, M. M.; Bao, D.; Wulan, B. R.; Li, Y. H.; Zhang, Y. F.; Yan, J. M.; Jiang, Q. Au sub-nanoclusters on TiO_2 toward highly efficient and selective electrocatalyst for N_2 conversion to NH_3 at ambient conditions. *Adv. Mater.* **2017**, *29*, 1606550.

[39] Howalt, J. G.; Vegge, T. Electrochemical ammonia production on molybdenum nitride nanoclusters. *Phys. Chem. Chem. Phys.* **2013**, *15*, 20957–20965.

[40] Xu, L.; Jiang, Q. Q.; Xiao, Z. H.; Li, X. Y.; Huo, J.; Wang, S. Y.; Dai, L. M. Plasma-engraved Co_3O_4 nanosheets with oxygen vacancies and high surface area for the oxygen evolution reaction. *Angew. Chem., Int. Ed.* **2016**, *55*, 5277–5281.

[41] Dou, S.; Tao, L.; Huo, J.; Wang, S. Y.; Dai, L. M. Etched and doped Co_9S_8/graphene hybrid for oxygen electrocatalysis. *Energy Environ. Sci.* **2016**, *9*, 1320–1326.

[42] Tian, G. L.; Zhang, Q.; Zhang, B. S.; Jin, Y. G.; Huang, J. Q.; Su, D. S.; Wei, F. Toward full exposure of "active sites": Nanocarbon electrocatalyst with surface enriched nitrogen for superior oxygen reduction and evolution reactivity. *Adv. Funct. Mater.* **2014**, *24*, 5956–5961.

[43] Sun, X. H.; Jiang, K. Z.; Zhang, N.; Guo, S. J.; Huang, X. Q. Crystalline control of {111} bounded Pt_3Cu nanocrystals: Multiply-twinned Pt_3Cu icosahedra with enhanced electrocatalytic properties. *ACS Nano* **2015**, *9*, 7634–7640.

[44] Tang, C.; Wang, H. F.; Chen, X.; Li, B. Q.; Hou, T. Z.; Zhang, B. S.; Zhang, Q.; Titirici, M. M.; Wei, F. Topological defects in metal-free nanocarbon for oxygen electrocatalysis. *Adv. Mater.* **2016**, *28*, 6845–6851.

[45] Xiao, Z. H.; Wang, Y.; Huang, Y. C.; Wei, Z. X.; Dong, C. L.; Ma, J. M.; Shen, S. H.; Li, Y. F.; Wang, S. Y. Filling the oxygen vacancies in Co_3O_4 with phosphorus: An ultra-efficient electrocatalyst for overall water splitting. *Energy Environ. Sci.* **2017**, *10*, 2563–2569.

[46] Kugler, K.; Luhn, M.; Schramm, J. A.; Rahimi, K.; Wessling, M. Galvanic deposition of Rh and Ru on randomly structured Ti felts for the electrochemical NH_3 synthesis. *Phys. Chem. Chem. Phys.* **2015**, *17*, 3768–3782.

[47] Logadottir, A.; Rod, T. H.; Nørskov, J. K.; Hammer, B.; Dahl, S.; Jacobsen, C. J. H. The Brønsted–Evans–Polanyi relation and the volcano plot for ammonia synthesis over transition metal catalysts. *J. Catal.* **2001**, *197*, 229–231.

[48] Ishikawa, A.; Doi, T.; Nakai, H. Catalytic performance of Ru, Os, and Rh nanoparticles for ammonia synthesis: A density functional theory analysis. *J. Catal.* **2018**, *357*, 213–222.

[49] Pickett, C.; Talarmin, J. Electrosynthesis of ammonia. *Nature* **1985**, *317*, 652–653.

[50] Furuya, N.; Yoshiba, H. Electroreduction of nitrogen to ammonia on gas-diffusion electrodes modified by Fe-phthalocyanine. *J. Electroanal. Chem. Interf. Electrochem.* **1989**, *263*, 171–174.

[51] Furuya, N.; Yoshiba, H. Electroreduction of nitrogen to ammonia on gas-diffusion electrodes modified by metal phthalocyanines. *J. Electroanal. Chem. Interf. Electrochem.* **1989**, *272*, 263–266.

[52] Shipman, M. A.; Symes, M. D. A re-evaluation of Sn(II) phthalocyanine as a catalyst for the electrosynthesis of ammonia. *Electrochim. Acta* **2017**, *258*, 618–622.

[53] Jeong, E. Y.; Yoo, C. Y.; Jung, C. H.; Park, J. H.; Park, Y. C.; Kim, J. N.; Oh, S. G.; Woo, Y.; Yoon, H. C. Electrochemical ammonia synthesis mediated by titanocene dichloride in aqueous electrolytes under ambient conditions. *ACS Sustainable Chem. Eng.* **2017**, *5*, 9662–9666.

[54] Hellman, A.; Baerends, E. J.; Biczysko, M.; Bligaard, T.; Christensen, C. H.; Clary, D. C.; Dahl, S.; van Harrevelt, R.; Honkala, K.; Jonsson, H. et al. Predicting catalysis: Understanding ammonia synthesis from first-principles calculations. *J. Phys. Chem. B* **2006**, *110*, 17719–17735.

[55] Dahl, S.; Logadottir, A.; Egeberg, R. C.; Larsen, J. H.; Chorkendorff, I.; Törnqvist, E.; Nørskov, J. K. Role of steps in N_2 activation on Ru (0001). *Phys. Rev. Lett.* **1999**, *83*, 1814–1817.

[56] Dahl, S.; Törnqvist, E.; Chorkendorff, I. Dissociative adsorption of N_2 on Ru (0001): A surface reaction totally dominated by steps. *J. Catal.* **2000**, *192*, 381–390.

[57] Strongin, D. R.; Carrazza, J.; Bare, S. R.; Somoriai, G. A. The importance of C_7 sites and surface roughness in the ammonia synthesis reaction over iron. *J. Catal.* **1987**, *103*, 213–215.

[58] Yang, D. S.; Chen, T.; Wang, Z. J. Electrochemical reduction of aqueous nitrogen (N_2) at a low overpotential on (110)-oriented Mo nanofilm. *J. Mater. Chem. A* **2017**, *5*, 18967–18971.

[59] Renner, J. N.; Greenlee, L. F.; Ayres, K. E.; Herring, A. M. Electrochemical synthesis of ammonia: A low pressure, low temperature approach. *Electrochem. Soc. Interface* **2015**, *24*, 51–57.

[60] Kong, J.; Lim, A.; Yoon, C.; Jang, J. H.; Ham, H. C.; Han, J.; Nam, S.; Kim, D.; Sung, Y. E.; Choi, J. et al. Electrochemical synthesis of NH_3 at low temperature and atmospheric pressure using a γ-Fe_2O_3 catalyst. *ACS Sustain. Chem. Eng.* **2017**, *5*, 10986–10995.

[61] Höskuldsson, Á. B.; Abghoui, Y.; Gunnarsdóttir, A. B.; Skúlason, E. Computational screening of rutile oxides for electrochemical ammonia formation. *ACS Sustainable Chem. Eng.* **2017**, *5*, 10327–10333.

[62] Furuya, N.; Yoshiba, H. Electroreduction of nitrogen to ammonia on gas-diffusion electrodes loaded with inorganic catalyst. *J. Electroanal. Chem. Interfac. Electrochem.* **1990**, *291*, 269–272.

[63] Lan, R.; Alkhazmi, K. A.; Amar, I. A.; Tao, S. W. Synthesis of ammonia directly from wet air using new perovskite oxide La$_{0.8}$Cs$_{0.2}$Fe$_{0.8}$Ni$_{0.2}$O$_{3-\delta}$ as catalyst. *Electrochim. Acta* **2014**, *123*, 582–587.

[64] Bruix, A.; Rodriguez, J. A.; Ramirez, P. J.; Senanayake, S. D.; Evans, J.; Park, J. B.; Stacchiola, D.; Liu, P.; Hrbek, J.; Illas, F. A new type of strong metal-support interaction and the production of H_2 through the transformation of water on Pt/CeO_2(111) and $Pt/CeO_x/TiO_2$(110) catalysts. *J. Am. Chem. Soc.* **2012**, *134*, 8968–8974.

[65] Qiao, B. T.; Wang, A. Q.; Yang, X. F.; Allard, L. F.; Jiang, Z.; Cui, Y. T.; Liu, J. Y.; Li, J.; Zhang, T. Single-atom catalysis of CO oxidation using Pt_1/FeO_x. *Nat. Chem.* **2011**, *3*, 634–641.

[66] Wang, R.; Xue, X. Y.; Lu, W. C.; Liu, H. W.; Lai, C.; Xi, K.; Che, Y. K.; Liu, J. Q.; Guo, S. J.; Yang, D. J. Tuning and understanding the phase interface of TiO_2 nanoparticles for more efficient lithium ion storage. *Nanoscale* **2015**, *7*, 12833–12838.

[67] Guo, S. J.; Zhang, X.; Zhu, W. L.; He, K.; Su, D.; Mendoza-Garcia, A.; Ho, S. F.; Lu, G.; Sun, S. H. Nanocatalyst superior to Pt for oxygen reduction reactions: The case of core/shell Ag(Au)/CuPd nanoparticles. *J. Am. Chem. Soc.* **2014**, *136*, 15026–15033.

[68] Farmer, J. A.; Campbell, C. T. Ceria maintains smaller metal catalyst particles by strong metal-support bonding. *Science* **2010**, *329*, 933–936.

[69] Wang, Y. H.; Cui, X. Q.; Zhang, Y. Y.; Zhang, L. J.; Gong, X. G.; Zheng, G. F. Achieving high aqueous energy storage via hydrogen-generation passivation. *Adv. Mater.* **2016**, *28*, 7626–7632.

[70] Abghoui, Y.; Garden, A. L.; Hlynsson, V. F.; Björgvinsdóttir, S.; Ólafsdóttir, H.; Skúlason, E. Enabling electrochemical reduction of nitrogen to ammonia at ambient conditions through rational catalyst design. *Phys. Chem. Chem. Phys.* **2015**, *17*, 4909–4918.

[71] Azofra, L. M.; Li, N.; MacFarlane, D. R.; Sun, C. H. Promising prospects for 2D d^2–d^4 M_3C_2 transition metal carbides (MXenes) in N_2 capture and conversion into ammonia. *Energy Environ. Sci.* **2016**, *9*, 2545–2549.

[72] Zhao, X. R.; Yin, F. X.; Liu, N.; Li, G. R.; Fan, T. X.; Chen, B. H. Highly efficient metal–organic-framework catalysts for electrochemical synthesis of ammonia from N_2 (air) and water at low temperature and ambient pressure. *J. Mater. Sci.* **2017**, *52*, 10175–10185.

[73] Abghoui, Y.; Garden, A. L.; Howat, J. G.; Vegge, T.; Skúlason, E. Electroreduction of N_2 to ammonia at ambient conditions on mononitrides of Zr, Nb, Cr, and V: A DFT guide for experiments. *ACS Catal.* **2016**, *6*, 635–646.

[74] Zhao, J. X.; Chen, Z. F. Single Mo atom supported on defective boron nitride monolayer as an efficient electrocatalyst for nitrogen fixation: A computational study. *J. Am. Chem. Soc.* **2017**, *139*, 12480–12487.

[75] Köleli, F.; Kayan, D. B. Low overpotential reduction of dinitrogen to ammonia in aqueous media. *J. Electroanal. Chem.* **2010**, *638*, 119–122.

[76] Kim, K.; Lee, N.; Yoo, C. Y.; Kim, J. N.; Yoon, H. C.; Han, J. I. Communication-electrochemical reduction of nitrogen to ammonia in 2-propanol under ambient temperature and pressure. *J. Electrochem. Soc.* **2016**, *163*, F610–F612.

[77] Kim, K.; Yoo, C. Y.; Kim, J. N.; Yoon, H. C.; Han, J. I. Electrochemical synthesis of ammonia from water and nitrogen in ethylenediamine under ambient temperature and pressure. *J. Electrochem. Soc.* **2016**, *163*, F1523–F1526.

[78] Ma, J. L.; Bao, D.; Shi, M. M.; Yan, J. M.; Zhang, X. B. Reversible nitrogen fixation based on a rechargeable lithium-nitrogen battery for energy storage. *Chem* **2017**, *2*, 525–532.

[79] Lan, R.; Irvine, J. T. S.; Tao, S. W. Synthesis of ammonia directly from air and water at ambient temperature and pressure. *Sci. Rep.* **2013**, *3*, 1145.

[80] Köleli, F.; Röpke, T. Electrochemical hydrogenation of dinitrogen to ammonia on a polyaniline electrode. *Appl. Catal. B* **2006**, *62*, 306–310.

[81] Lan, R.; Tao, S. W. Electrochemical synthesis of ammonia directly from air and water using a $Li^+/H^+/NH_4^+$ mixed conducting electrolyte. *RSC Adv.* **2013**, *3*, 18016–18021.

[82] Schrock, R. R. Catalytic reduction of dinitrogen to ammonia at a single molybdenum center. *Acc. Chem. Res.* **2005**, *38*, 955–962.

[83] Anderson, J. S.; Rittle, J.; Peters, J. C. Catalytic conversion of nitrogen to ammonia by an iron model complex. *Nature* **2013**, *501*, 84–87.

[84] Arashiba, K.; Miyake, Y.; Nishibayashi, Y. A molybdenum complex bearing PNP-type pincer ligands leads to the catalytic reduction of dinitrogen into ammonia. *Nat. Chem.* **2010**, *3*, 120–125.

[85] Jackson, M. N.; Surendranath, Y. Donor-dependent kinetics of interfacial proton-coupled electron transfer. *J. Am. Chem. Soc.* **2016**, *138*, 3228–3234.

[86] Christensen, C. H.; Johannessen, T.; Sørensen, R. Z.; Nørskov, J. K. Towards an ammonia-mediated hydrogen economy? *Catal. Today* **2006**, *111*, 140–144.

[87] Lan, R.; Tao, S. W. Ammonia as a suitable fuel for fuel cells. *Front. Energy Res.* **2014**, *2*, 35.